


Surface Nanopatterned Shape Memory Alloy (SMA)-Based Photosensitive Artificial Muscle

Journal Article

Author(s):

[Kim, Min-Soo](#) ; Lee, Hye-Sung; Cho, Younggyun; Heo, Jae Kyung; Quan, Ying-Jun; Lee, Seung Woo; Pahk, Heui Jae; Ahn, Sung-Hoon

Publication date:

2022-03-04

Permanent link:

<https://doi.org/10.3929/ethz-b-000522452>

Rights / license:

[Creative Commons Attribution-NonCommercial-NoDerivatives 4.0 International](#)

Originally published in:

Advanced Optical Materials 10(5), <https://doi.org/10.1002/adom.202102024>

Surface Nanopatterned Shape Memory Alloy (SMA)-Based Photosensitive Artificial Muscle

Min-Soo Kim, Hye-Sung Lee, Younggyun Cho, Jae Kyung Heo, Ying-Jun Quan, Seung Woo Lee, Heui Jae Pahk, and Sung-Hoon Ahn*

Light-driven shape memory alloy (SMA)-based microscale actuators show great promise for artificial muscle and biomedical applications, as they are actuated remotely and have a fast response speed. However, ultraviolet (UV) light is required for device actuation; thus, the operating environment has been limited. Here, an infrared (IR) light-driven SMA actuator is proposed, in which the plasmonic effect is used to enhance IR light absorptance. A sub-micrometer pattern is used to create an optical meta-surface capable of tuning the light absorptance. Conical nanohole arrays are fabricated with a focused ion beam. The absorptance tuning effect is evaluated in terms of the optical characteristics and performance of the actuator. The nanopatterned surface increases the narrow-band IR light absorption by up to 55%. Optics simulations are conducted to verify the experimental results. A pattern design method is proposed, based on the light wavelength of the stimulating source. Combining heterogeneous surfaces, both UV and IR light achieve decoupled microscale actuation. These actuators show a response similar to that of the iris muscle, which is responsible for the eye's pupillary reflex. It is expected that these actuators will broaden SMA applications in clinical devices and soft robotics.

1. Introduction

Stimuli responsive-smart materials have been widely utilized as actuation sources of artificial muscles^[1] and intelligent machines.^[2] These materials are responsive to light, temperature, electricity, or magnetic field.^[3] Since light sources can remotely transfer energy to a specific site,^[4] photosensitive actuators have been developed based on shape memory alloys (SMAs) and shape memory polymers (SMPs). Owing to the advantage of soft material, 3D-shaping, and printing-based manufacturing process, SMP was employed in microscale soft robots^[5] by 4D printing technique.^[4,6] On the other hand, SMA actuators can offer a high energy density, durability, and biocompatibility.^[7,8] Remarkably, as the size of the SMA structure decreases to the microscale, not only does the actuator show shape recovery, but also response speed increases sharply

due to the scale effect.^[9] Furthermore, using a laser as a remote thermal energy source simplifies the actuator design, as additional supply circuits are no longer necessary. These advantages allow small device configurations and miniaturization in biomedical applications.

In previous studies, ultraviolet (UV) lasers were used for microscale actuator heating;^[9,10] however, UV light sources are less biocompatible, which may pose problems in biomedical applications. Visible and infrared (IR) light can be used;^[11] however, compared with UV light, these wavelengths are not optimal in terms of the light absorptance of the SMA.^[12] In summary, UV light is an efficient energy source but is not biocompatible. Therefore, to achieve both biocompatibility and energy efficiency, the light absorptance of the photothermal SMA actuator must be enhanced for visible and IR wavelengths. This can be achieved through surface modification.


Surface modification, such as pattern formation, assigns particular characteristics to the surface only, i.e., not to the material bulk.^[13] If the period of the pattern decreases to the sub-micrometer scale, the surface becomes an optical meta-surface, which has a distinct electromagnetic response from that of the original material;^[14] examples of this include optical antennas,^[15] sensors,^[16] and bandpass filter and lens^[17] applications that operate based on plasmonic effects. In addition, light trapping has been used to enhance photon absorption, which

M.-S. Kim
Soft Robotics Research Center
Seoul National University
Seoul 08826, Republic of Korea

M.-S. Kim
Institute of Robotics and Intelligent Systems
ETH Zurich
Zurich CH-8092, Switzerland

H.-S. Lee, Y. Cho, J. K. Heo, S. W. Lee, H. J. Pahk, S.-H. Ahn
Department of Mechanical Engineering
Seoul National University
Seoul 08826, Republic of Korea
E-mail: ahnsh@snu.ac.kr

Y.-J. Quan, H. J. Pahk, S.-H. Ahn
Institute of Advanced Machines and Design
Seoul National University
Seoul 08826, Republic of Korea

 The ORCID identification number(s) for the author(s) of this article can be found under <https://doi.org/10.1002/adom.202102024>.

© 2021 The Authors. Advanced Optical Materials published by Wiley-VCH GmbH. This is an open access article under the terms of the Creative Commons Attribution-NonCommercial-NoDerivs License, which permits use and distribution in any medium, provided the original work is properly cited, the use is non-commercial and no modifications or adaptations are made.

DOI: 10.1002/adom.202102024

in turn improves the efficiency of photovoltaic platforms.^[18] In recent decades, there have been many advances in meta-surface designs for various optical devices and sensors; however, actuation platforms for these devices have developed more slowly.

As discussed earlier, plasmonic effects can be induced by making patterns on the surface, or by depositing thin films. Zaidi et al. introduced a color filter fabricated by plasma-enhanced chemical vapor deposition (PE-CVD),^[19] however, their approach provided only localized microscale absorptance changes. Further, the PE-CVD process is more involved, as pattern creation requires the use of a mask, which must be fabricated and precisely aligned. Conversely, surface patterning uses a single material, which avoids issues associated with material compatibility and delamination.

Given that coloration, a plasmonic effect, is due to the absorption and reflection of different light wavelengths, we propose SMA actuation using IR laser irradiation. As an optical meta-surface, conical nanohole arrays were fabricated in the SMA surface via a focused ion beam (FIB) process, to create nanoscale to microscale array structures.^[20] We experimentally observed the relationships among absorptance tuning effects, nanohole geometry, and FIB processing parameters. Finite-difference time-domain (FDTD) simulation results were compared with our experimental results, and showed good agreement. The nanopattern design could be customized to achieve the appropriate pattern period for high absorptance at a particular wavelength. In addition, the optical properties of nitinol (nickel–titanium alloy, an SMA) were identified by ellipsometry. The developed meta-surfaces were applied to microactuators. Actuation performance was evaluated both experimentally and theoretically with UV and IR laser irradiation. Furthermore, with a combination of heterogeneous surfaces, we achieved decoupled motion via IR and UV laser heating at the microscale in the first trial.

2. Results

2.1. Photosensitive SMA Actuator

Figure 1 shows a conceptual diagram of a photosensitive SMA actuator. The actuator configuration was inspired by the iris muscle of the eye, which constricts as a reflex to incoming light intensity. As opposed to an electrical signal inducing contraction of the muscle cells, the actuator does so via the photothermal effect. Thus, the light power and absorptance control the temperature, which determines the extent of the shape recovery (**Figure 1b**). In addition, the surface nanopattern induces a plasmonic effect that is used to tune the light absorptance. Therefore, a combination of different light absorptance surfaces leads to localized shape recovery resulting in asymmetric actuation at the microscale (**Figure 1c**). Using this design prototype, our photosensitive actuator would be applicable as an actuation source in miniaturized medical devices and microrobots requiring complex motion.

To demonstrate the suggested concept, we prepared an actuator prototype comprised of six bending elements (**Figure 2a**). The length, width, and thickness of the frame were 60, 5, and

5 μm , respectively. The minimum radius of curvature was set at 6.3 μm . The proposed frame structure enlarged the actuation strain under uniform shape deformation through stretching (**Figure S1**, Supporting Information). This is attributed to the detwinned martensite structure created over a large portion of the volume, which enhances the actuation strain when the shape is recovered.

Both non-patterned and nanopatterned surfaces were prepared to examine the effect of nanopatterns on the optical properties. The non-patterned surface (**Figure 2d,f**) was polished. The nanopatterned surface (**Figure 2e,g**) had a 700 nm periodic nanohole array. An FIB method was used to fabricate the actuators and nanopatterns.

In terms of actuation strain, we evaluated actuation performance using a micromanipulation system (**Figure 2a**). A micro-gripper held the end of the structure and stretched it by 20 μm . When the gripper was released, the structure shrank approximately 8.9 μm via a spring back effect and maintained a total length of 69.7 μm (**Figure 2c**). This was followed by heating with IR laser irradiation (wavelength: 785 nm; intensity: 2 W mm^{-2}), which triggered shape recovery. From optical microscopic images, the patterned surface showed 9.6 μm of displacement (16.0% actuation strain, **Figure 2d**), while the non-patterned surface showed 6.4 μm of displacement (10.6% actuation strain, **Figure 2e**). Under UV laser irradiation, there was no significant difference in actuation strain at patterned and non-patterned actuators.

Figure 2b summarizes the effect of the pattern and laser intensity on the actuation strain; the line indicates the experimental results, and the colored area corresponds to the theoretically estimated strain. The entire procedure was the same, except for the stretching length. The total length was set as 67.5 μm before heating. Our experimental results showed that the nanopattern affected actuation strain. The non-patterned actuator required two-fold the intensity to achieve the same amount of strain obtained by the patterned actuator. Especially, under 1 W mm^{-2} of laser intensity, the non-patterned actuator deformed by 1.3% of strain; however, the patterned actuator deformed by 7.5% (5.8 times). The actuation strain saturated at 12.5% as the laser intensity increased. Generally, nitinol maintains a thermomechanical property over cycles.^[8] In addition, the microscale SMA actuator showed actuation performance without significant degradation of performance over 5000 cycles.^[9] We also observed that the actuator showed comparably constant deformation length in 24 cycles of shape recovery (**Figure 2h,i**).

Finite element analysis was used to verify that the surface nanopattern changed the thermal energy input, which controls the temperature of the structure. We assumed that the input laser was fully converted to thermal energy and set the input intensity in consideration of the light absorptance. The surface 150 μm away from the structure was set at 20 °C, and natural convective heat transfer was assigned at every surface (**Figure S2**, Supporting Information). The arc was defined as the centerline of the structure. Then, we estimated strain under the assumption that deformation fully recovers with an arc length at which the temperature exceeds the shape-changing temperature (**Figure S3**, Supporting Information). The upper line of the colored area in **Figure 2b** corresponds to the predicted

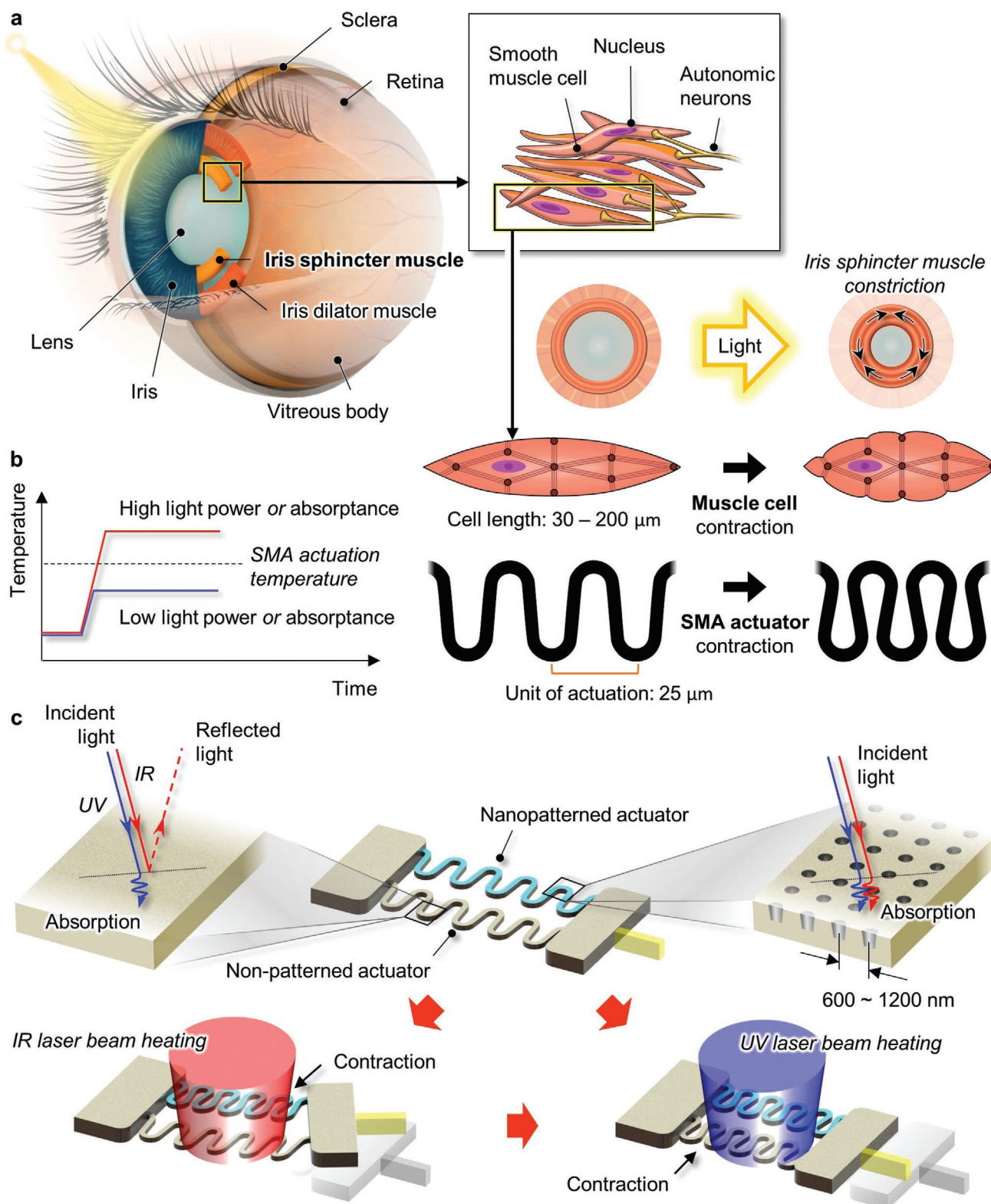


Figure 1. Schematic diagram of bio-inspired photosensitive shape memory alloy (SMA) actuator. a) The conceptual design of the SMA actuators employed as a photosensitive artificial muscle inspired by the iris muscle of the eye. b) Temperature control mechanism triggering SMA actuation by tuning the light intensity and absorbance. c) Conceptual diagram of a heterogeneous surface combination in a microscale actuator, with sequential motion performed via infrared (IR) and ultraviolet (UV) laser heating. The light absorption properties are determined by the nanopattern configuration.

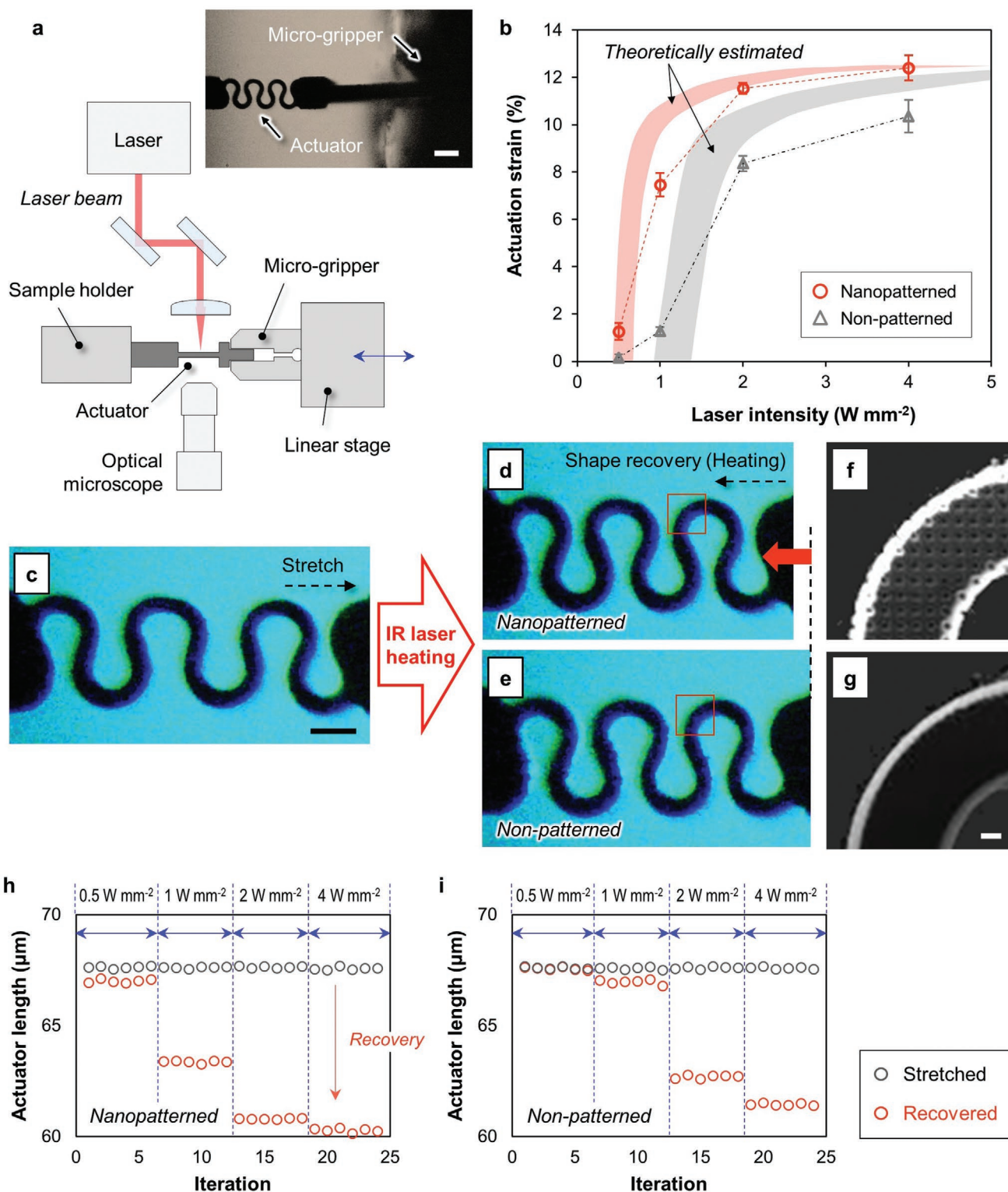


Figure 2. Photosensitive actuation strain change by laser intensity and surface nanopattern. a) SMA actuator and micromanipulation setup for evaluating actuation performance (scale bar: 20 μm). b) Comparison between the experimental and numerical results of the actuation strain against laser intensity for each surface. c) Optical microscopic image taken after actuator stretching (scale bar: 10 μm). d, e) Contraction caused by shape recovery, triggered by IR laser heating (intensity: 2 W mm^{-2}). The nanopatterned actuator showed an actuation strain 1.5-fold that of the non-patterned actuator. f, g) Scanning ion microscopy (SIM) images taken from the red square in (d, e) (scale bar: 1 μm). h, i) Actuator length change (deformation) as a function of iteration in cycle test. The initial actuator length was 60 μm .

strain when the shape-changing temperature coincided with the austenite starting temperature (A_s , 90 °C); the lower line is the predicted strain of the austenite finishing temperature (A_f , 110 °C). The phase of the SMA did not transform at a specific temperature; rather, the transformation took place continuously over the A_s – A_f temperature range, ultimately resulting in 5% actuation strain. For this reason, the estimated strains are presented as an area.

Given that both the experimental and theoretical results showed similar values and trends, we confirmed that the temperature distribution induced by laser heating was the main factor controlling actuation strain. Also, the proposed photo-sensitive mechanism was verified. Manufacturing error, subtle misalignment of the sample and laser optics, and laser intensity instability may explain the discrepancies between the (lower) experimental values and theoretical values.

Interestingly, the response of the actuator was similar to that of an iris muscle. The iris muscle comprises the iris sphincter muscle, which contracts under high light intensity, and the iris dilator muscle, which contracts under low light intensity. Pupil light reflex, a method used to determine the consciousness of a person, occurs when the iris sphincter muscle constricts by sensing the light intensity. This is a parasympathetic reflex, in which the sensory neurons (sensors), midbrain (processors), and muscles (actuators) work in combination. However, many sub-primates, such as mice, have an intrinsic mechanism in which muscles contract in response to light without synaptic transmission. In other words, the iris sphincter muscle of the mouse is photosensitive.^[21] As a result, this organic system has the advantage of being tiny and simple, and operates independently of cognitive processes.

Likewise, the developed actuator showed controllable actuation strain that depended on the light intensity, without the need for additional sensors or processing devices. Thus, the developed actuator was comparable to the iris sphincter muscle in terms of its behavior, actuation performance, and dimensions (Table 1). However, this actuator is also more advanced than the iris muscles, as it is more spectrum-sensitive. In terms of performance and behavior, the developed actuators are promising for use in self-photosensing artificial muscle devices. In other words, we expect that they can be a spectrum-sensitive programmable actuator to implement the intelligent machine, which is an extended concept of artificial intelligence.^[2,22]

Table 1. Comparison of iris sphincter muscle and the photosensitive SMA actuator.

Specification	Iris sphincter muscle	Photosensitive SMA actuator
Actuation strain	0.2–0.25	0.16
Actuation stress (MPa)	0.005–0.05 ^[21,23]	0.75 ^[9]
Diameter (μm)	1–5	25
Length (μm)	30–200 (Muscle cell)	25 (Unit of actuation)
Maximum deformation ratio	0.15–0.6 ^[24]	0.28 ^{a)}

^{a)}Details in supporting information Note S3.

2.2. Surface Nanopattern on Shape Memory Alloy

2.2.1. Geometry of the Nanohole Array

The shape and dimensions of the nanopattern were the main factors determining light absorptance. When a pattern is fabricated using an FIB process, the resulting nanohole is generally conical in shape; however, the exact dimensions are determined naturally by the reaction between the ion beam and the material. Thus, it is necessary to analyze nanohole geometries as a function of the FIB processing parameters. We investigated nanohole geometries that varied with the ion dose conditions (acceleration voltage: 30 keV; probe current: 150 and 300 pA) and dwell time (0.2, 0.4, 0.8, and 1.6 s) by fabricating nanopattern arrays 70 × 70 μm² in size. The pattern period was set at 700 nm.

Figure 3a,b show top and cross-sectional views of the fabricated nanopattern, respectively. To acquire the exact hole geometries from the cross-sectional view analysis, we deposited platinum onto the patterns by sputtering, before obtaining cross-sectional images. The pattern was uniformly fabricated with a period of 707 ± 71 nm. Figure 3c,d show the variation in nanohole geometry according to the processing conditions.

Figure 3e shows the trend in the diameter and depth changes as a function of dwell time. The depth increased from 257 to 911 nm under 150 pA ion beam conditions, and from 355 to 1511 nm at 300 pA. The diameter increased from 407 to 545 nm at 150 pA, and from 513 to 692 nm at 300 pA. As the dwell time increased, the depth increased exponentially up to 0.8 s and then plateaued; this was attributed to redeposition as the hole deepened. Thus, the processing conditions significantly affected the hole geometry. Similar hole diameters were achieved under 150 pA/0.8 s and 300 pA/0.2 s conditions; this was also the case for the holes created under 150 pA/1.6 s and 300 pA/0.4 s conditions. Additionally, a greater depth was achieved using 300 pA/0.8 s compared with 150 pA/1.6 s conditions. Next, we will consider the effect of the nanohole geometry on light absorptance.

2.2.2. Tuning Light Absorptance at Spectrum

The surface nanopattern tunes the light absorptance via a plasmonic effect (i.e., surface plasmon resonance, SPR), which manifests as coherent delocalized electron oscillations in a thin metallic film with dielectric interfaces. SPR is rendered by the nanopatterned surface.^[15,25] As such, we investigated the relationship between light absorptance and the nanohole geometries in both simulations and experiments.

FDTD analysis was carried out based on the material properties, geometry, and boundary conditions. Although the refractive index is related to the material properties, it has not been strongly established in various materials. To increase the accuracy of the FDTD simulations, the refractive index for nitinol was measured using an ellipsometer (Note S1 and Figure S4, Supporting Information).^[26] According to the geometry revealed by scanning electron microscopy (SEM) images, the nanoholes were modeled in three dimensions. Symmetric boundary conditions (i.e., a period of 700 nm) reduced the numerical

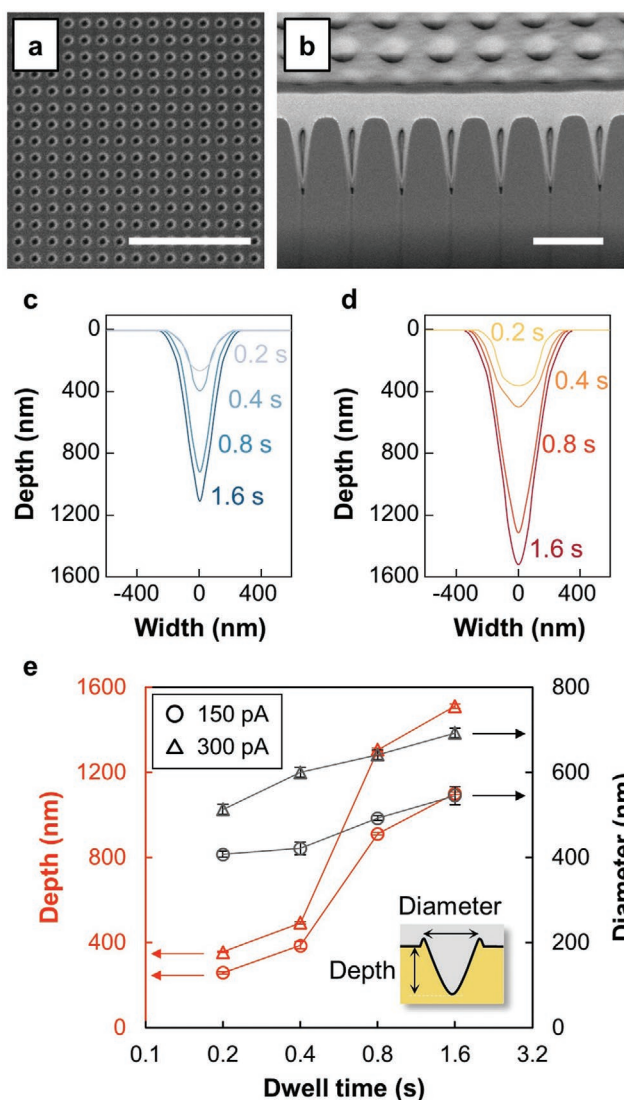


Figure 3. Nanohole geometry analysis. a) Scanning electron microscopy (SEM) image of the nanopattern taken in top view, showing a uniform nanohole array (scale bar: 5 μm). b) SEM image of the cross-sectional view, showing the nanohole geometry (scale bar: 1 μm). c,d) The nanohole geometries created by varying the ion beam probe current (left: 150 pA, right: 300 pA) and dwell time (0.2, 0.4, 0.8, and 1.6 s). e) Hole diameter and depth as a function of dwell time.

calculation time. Light irradiated the SMA surface at normal incidence. The reflected light was measured by a monitor positioned parallel to the surface. Absorptance was calculated using Equation (1), as follows:

$$A(\lambda) = 1 - R(\lambda) - T(\lambda) \quad (1)$$

where A , R , T , and λ represent the absorptance, reflectance, transmittance, and wavelength of light, respectively. When the SMA thickness exceeded 1 μm , the transmittance was assumed to be 0.

Figure 4a shows an example of the simulated light behavior, in which the nanoholes have the same geometry as those

fabricated under 300 pA/0.4 s conditions. A comparison of the non-patterned and nanopatterned surfaces under 785 nm light irradiation showed that the flat surface absorbed 45% of the light and reflected 55%. In contrast, the nanopatterned surface absorbed most of the light, with little or no light reflection.

Figure 4d,e show the simulation results, ranging from 400 to 900 nm of the light spectrum. Under strong ion beam irradiation, the light absorptance increased in the proximity of 780 nm. The absorptance showed similar patterns under the 150 pA/0.8 s and 300 pA/0.2 s conditions, as well as the 150 pA/1.6 s and 300 pA/0.4 s conditions. With respect to the nanohole geometry, our results indicated that the nanohole diameter played a bigger role in light absorptance than the depth.

We also experimentally evaluated light absorptance over the wavelength range of 400 to 900 nm (Figure 4b,c). The reflectance was measured with a spectrometer, and the absorptance was then calculated using Equation 1. Similar to the simulation results, the absorptance of 740–790 nm light increased with the dwell time. The peak appeared over the same wavelength range. However, in the case of a 300 pA beam current, the light absorptance increased over most of the spectrum for dwell times exceeding 0.8 s. The pattern geometry led to different colors (Figure S5, Supporting Information); specifically, the color shifted from yellow to green with a 150 pA beam current and from green to black with a 300 pA beam current. The colors associated with the 150 pA/1.6 s and 150 pA/0.8 s conditions were similar to those obtained under the 300 pA/0.4 s and 300 pA/0.2 s conditions. In the case of the surface fabricated at 300 pA for 1.6 s, it appeared that most of the light spectrum was absorbed. Meanwhile, the experimental results showed a broader peak and lower amplitude than the theoretical estimations. This may be due to the gathering of light by the objective lens. Other errors might include fabrication errors, such as redeposition or misalignment in the measurement setup.

According to both the theoretical and simulation results, the absorptance of IR light increased from 46% to 90%. From this, we concluded that absorptance tuning enhanced the actuation performance of the SMA actuators by changing the nanopattern. Also, the difference in absorptance between IR light and other parts of the spectrum allowed the actuator to effectively distinguish the shape recovery induced by the different light sources. The difference was as large as 30% in the 150 pA/1.6 s and 300 pA/0.4 s patterns. Therefore, in terms of maximizing productivity, the optimal processing parameters would be 300 pA and a dwell time of 0.4 s.

The FDTD simulation results not only support the measurement results, but also underscore the importance of pattern design. We can design patterns according to the desired active wavelength of the light source. Figure 4f shows the change in absorptance at each wavelength as a function of the pattern period. If the laser source is fixed, the equation can be used to determine the period of the pattern. For example, a 1244 nm period pattern can be used with 1064 nm laser irradiation. Moreover, a combination of heterogeneous lasers and surfaces can be used to generate more complex decoupled motion (Figure 1c).

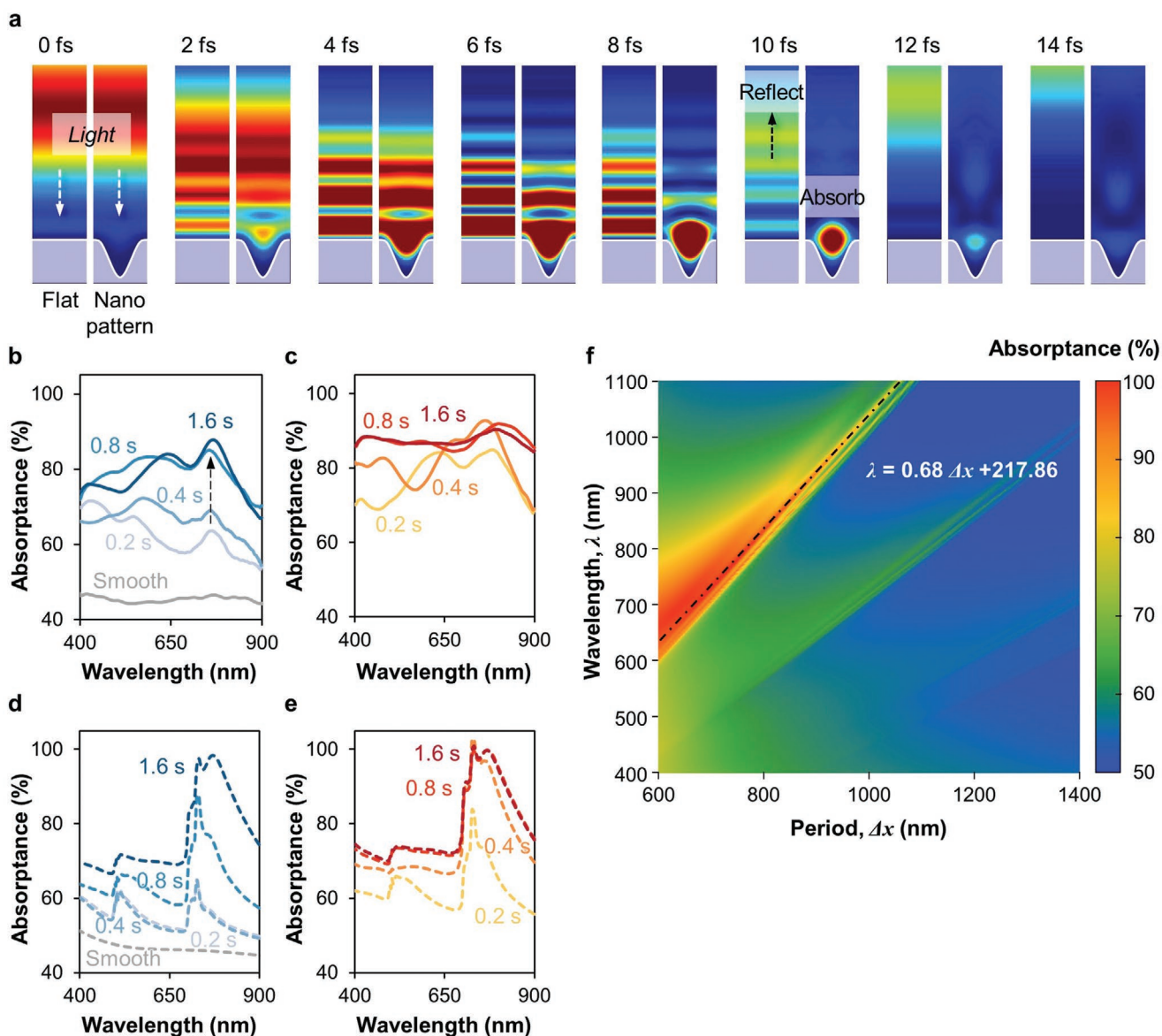


Figure 4. Light absorbance of SMA metasurface. a) Finite-difference time-domain (FDTD) simulation of light propagation over time. Light (wavelength: 785 nm) was reflected at the non-patterned surface but absorbed at the nanopatterned surface. b, c) Experimental results for light absorbance, which varied depending on the processing conditions (left: 150 pA, right: 300 pA, dwell time: 0.2–1.6 s). The higher ion dose condition increased the light absorbance around 785 nm. d, e) Numerical results obtained by FDTD simulations (left: 150 pA, right: 300 pA; dwell time: 0.2–1.6 s). f) The absorbance varied with the period of the nanopattern. Based on the estimations, it is possible to choose a period that ensures high absorbance at a specific wavelength.

2.3. Heterogeneous Surface Combination

Based on the heterogeneous surface combination concept, we developed actuators having both non-patterned and patterned surfaces. First, heterogeneous surfaces were introduced in a single S-bend-shaped frame actuator, as well as in double actuators.

2.3.1. Heterogeneous Surface on a Single Actuator

Figure 5a,b show the combination of both patterned and non-patterned surfaces in a single actuator. The actuator was 60 μm

long and stretched 5 μm (8.3%). Then, the IR laser and UV laser were irradiated sequentially to induce the shape memory effect. For a set UV laser intensity of 2 W mm^{-2} , the actuator behavior was evaluated as the IR laser intensity was varied from 0.5 to 4 W mm^{-2} . Sequential shape changes were induced with 1 W mm^{-2} of IR exposure; however, the shape recovered at once under 4 W mm^{-2} of IR heating. No change was observed with UV heating.

We quantitatively analyzed the motion of the actuator by image processing. The image was acquired with a 30-Hz sampling frequency, and the right rectangular part of the actuator was traced (Figure 5c and Figure S6, Supporting Information). Figure 5d shows the motion in the x and y directions. Figure 5e

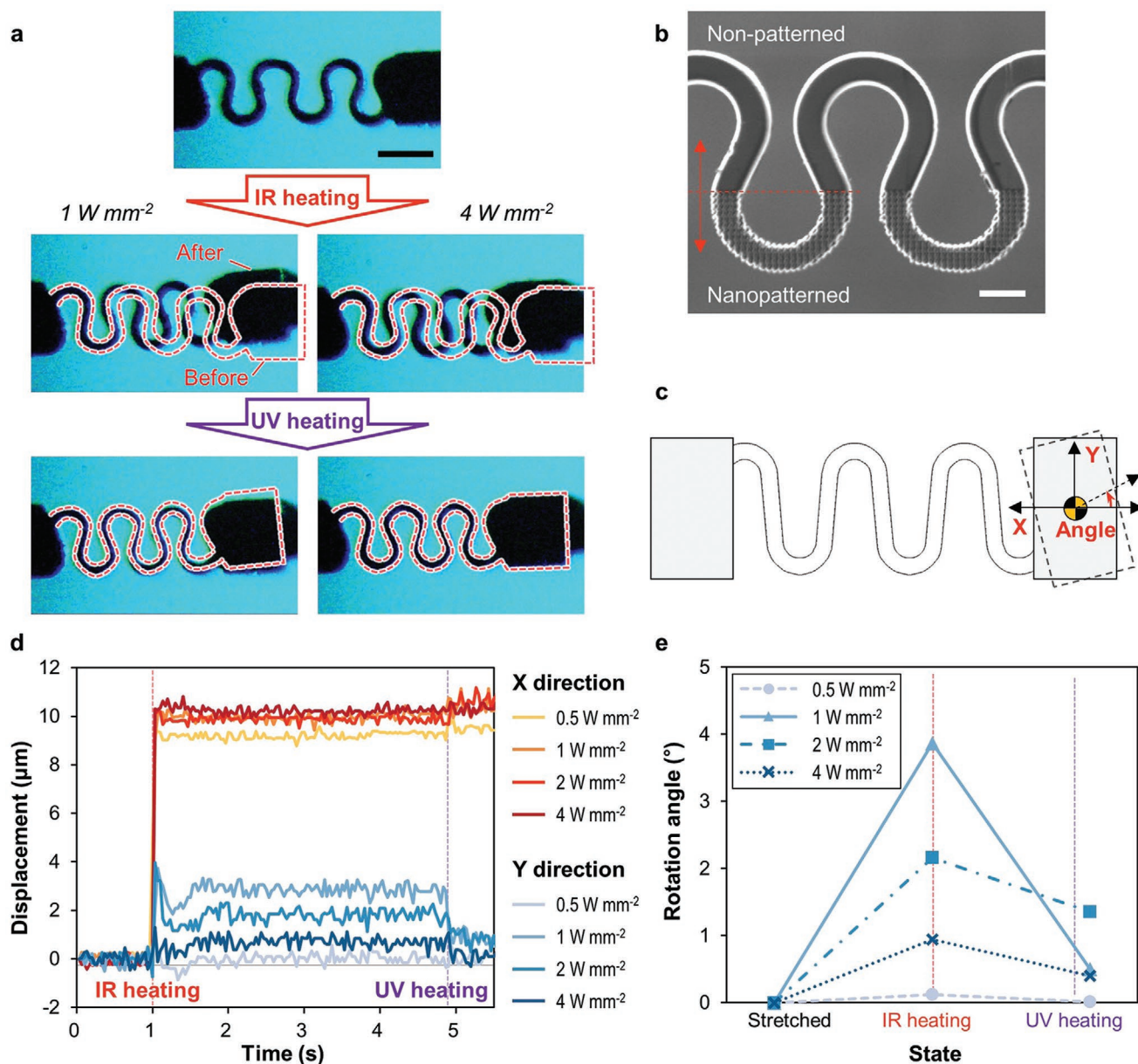


Figure 5. Heterogeneous surface combination on a single actuator. a) Optical microscopic image of a single actuator having a non-patterned and nanopatterned surface. The actuator showed sequential motion with 1 W mm^{-2} IR laser heating, but constricted at once with 4 W mm^{-2} laser exposure (scale bar: $20 \mu\text{m}$). b) SIM image of the actuator. The top half was non-patterned and the bottom half was nanopatterned (scale bar: $5 \mu\text{m}$). c) Schematic diagram explaining the directions and angle in (d,e). d) Actuation displacement as a function of the laser intensity ($0.5\text{--}4 \text{ W mm}^{-2}$). e) Rotation angle with respect to the laser intensity ($0.5\text{--}4 \text{ W mm}^{-2}$); 1 W mm^{-2} of laser intensity decoupled the motion via IR and UV heating.

shows the rotating angle as a function of the heating source. The most effective setting for decoupled motion was 1 W mm^{-2} of IR laser intensity, which induced a change in displacement of $3.0 \mu\text{m}$ (actuation strain: 12%) in the y-direction and a 4° change in the angle. Full shape recovery was not observed when the IR laser intensity was less than 0.5 W mm^{-2} . Above 2 W mm^{-2} of intensity, the non-patterned surface also heated up; thus, a single actuator was capable of achieving sequential shape change at the microscale under 1 W mm^{-2} of combined IR and UV heating.

2.3.2. Heterogeneous Surface on Two Actuators

A combination of two actuators having different surfaces achieved sequentially decoupled motion without exquisite intensity control. Two S-bend-shaped frame actuators were fabricated. The upper actuator was engraved with the nanopattern (Figure 6a). The actuator was $40 \mu\text{m}$ long and stretched $5 \mu\text{m}$ (12.5%, Figure 6b,c). Heating with a 2 W mm^{-2} IR laser caused the nanopatterned actuator to shrink by $1.5 \mu\text{m}$ (Figure 6d). The right side of the rectangular part rotated 4° in response.

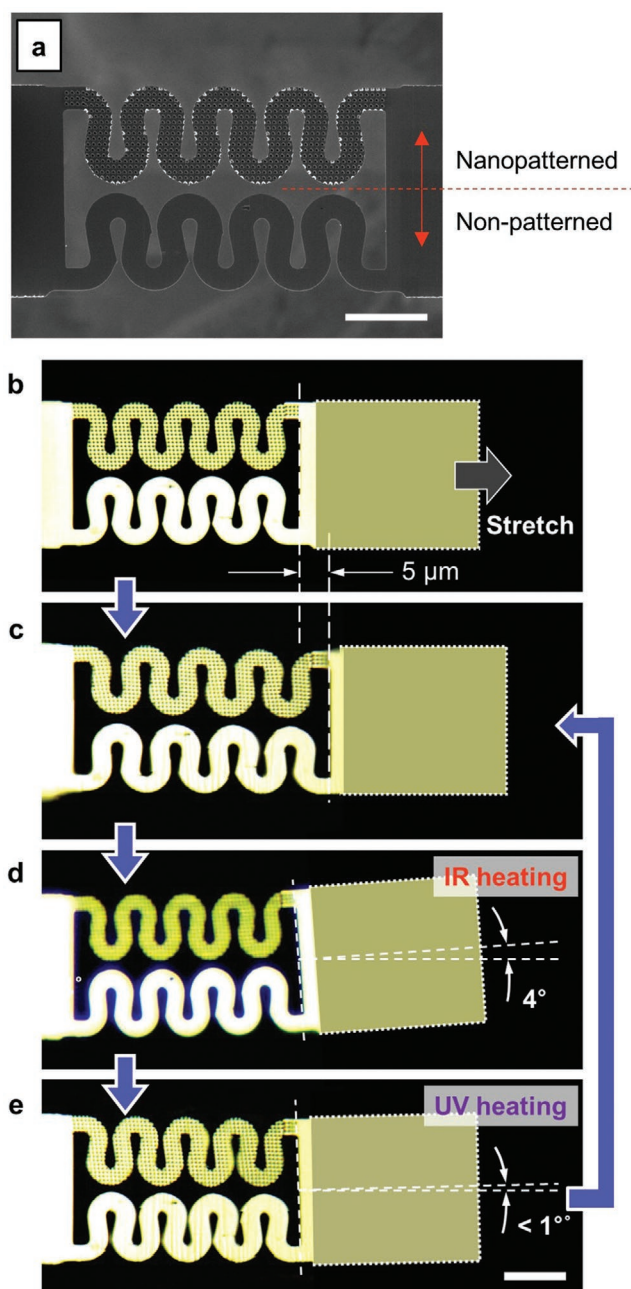


Figure 6. Heterogeneous surface combination on two actuators. a) SIM image of the two-actuator combination having nanopatterned and non-patterned surfaces (scale bar: 10 μm). b–e) Optical microscopic images taken during a stretch, IR heating, and UV heating (scale bar: 10 μm).

The lower actuator contracted under the UV laser heating (Figure 6e). Finally, the actuator recovered to its original shape with a small redundant shape change.

We achieved sequential motion at the microscale using both methods. According to the surface combination method, there was a trade-off with respect to the complexity of the laser system and the actuator design. By incorporating different surfaces into one actuator, we can reduce the actuator size; however, sensitive intensity control is necessary to decouple sequential motion. In contrast, when utilizing two actuators, the laser

system can be simplified; however, a larger space is required. Future customization of the actuator could provide the desired conditions for applications.

3. Conclusion

In summary, we demonstrated the concept of a photosensitive microscale SMA actuator that enhances visible and IR light absorptance via a nanopattern plasmonic effect. The main goal of this research was to apply a simple nanopattern not only to develop a biocompatible heating method but also to implement microscale asymmetric motion. Unlike the color filter method, this concept does not require the use of two or more materials, so delamination is much less problematic. In addition, the localized plasmonic effect enables absorptance tuning over a small area. In terms of manufacturing, the FIB process is a flexible, single-step fabrication method for creating localized patterns without a mask; the actuator and pattern design can be customized for the desired effect. In this research, to evaluate and improve the effect of the nanopatterns, the nanohole geometry and optical properties were analyzed experimentally and numerically. The nanohole diameter was one of the main parameters to obtain a significant absorptance difference. In addition, FDTD simulation results showed that the pattern period can be customized for a particular wavelength having a high absorptance. Finally, the actuation strain verified the plasmonic effect on the photothermal actuator. In addition, a combination of heterogeneous surfaces was used to demonstrate sequential microscale motion as a response to IR and UV laser heating.

Our actuator design shows great potential for use as an actuation source for artificial muscles and/or in combination with other built-in sensors and processes. Based on the improvement of the manufacturing process to pattern in higher resolution, using various wavelength lasers can achieve the advanced programmable actuator demonstrating complicated motion. In addition, although photo-sensitive actuation was performed by using high-temperature nitinol in this research, this concept can be applied to nitinol with a low actuation temperature (35–40 °C). The biocompatibility and high energy density properties of nitinol along with the developed optical meta-surface, broaden the applications of photothermal SMA actuators in biomedical platforms, to encompass minimally invasive surgery end effectors and microrobots. Furthermore, we expect that the developed photo-sensitive actuator contributes to implementing intelligent machines having combined functions of sensing, decision-making, controlling, and acting.^[2,22,27]

4. Experimental Section

Fabrication of the Microscale Actuator and Nanopattern via FIB: The metasurface and actuator were fabricated on a 25.6 μm diameter SMA wire (Flexinol actuator wire; Dynalloy, Inc., Irvine, CA, USA) via FIB milling (FIB column: COBRA; Orsay Physics, Fuveau, France; FIB stage: UST-5100; E Field Co. Inc., Billerica, MA, USA). After fabricating a flat thin film, the wire was rotated 90°. Then, the S-bend shape was created, and the nanoscale conical hole array was engraved. To make an S-bend spring, a 512 × 512 bitmap image was used under a 2500-pA beam current (acceleration voltage: 30 keV). The nanopattern produced

depended on the ion dose conditions (acceleration voltage: 30 keV, probe current: 150 pA, 300 pA); dwell time (0.2, 0.4, 0.8, or 1.6 s).

Optical Property Measurements: Using an optical system comprised of a halogen light source, an optical microscope (objective lens: CF Plan: 2.5×, NA: 0.075; Nikon, Tokyo, Japan), and a spectrometer (Maya 2000 Pro; Ocean Optics Inc., Largo, FL, USA), the reflected light intensity was measured. The light was directed perpendicular with respect to the surface, and the reflected light was detected at normal incidence. The reflected light intensity was estimated by comparing it with the intensity of a silver mirror reference.

Micromanipulation: The micromanipulation system comprised a three-axis (X, Y, and Z) nanopositioner and a microgripper (SG-1730; SmarAct GmbH, Oldenburg, Germany). The video was captured using a charge-coupled device camera (acA1920-155uc; Basler Ace, Ahrensburg, Germany) assembled in the microscopy system (objective lens: CF Plan: 20×, NA: 0.4; Nikon). For the heating source, a UV laser (wavelength: 355 nm; Awave355-4W30K was utilized; Advanced Optowave Co., Ronkonkoma, NY, USA) and an IR laser (wavelength: 785 nm; Stradus 785-80; Vortran Laser Technology, Inc., Roseville, CA, USA).

Supporting Information

Supporting Information is available from the Wiley Online Library or from the author.

Acknowledgements

The authors thank Wongyeong Heo for his assistance with an illustration. This work was supported by the National Research Foundation of Korea (NRF) grants funded by the MSIT (NRF-2021R1A2B5B03087094, NRF-2020R1A6A3A03037461), the Basic Research Lab Program through the National Research Foundation of Korea (NRF) funded by the MSIT (NRF-2021R1A4A2001824), the Institute of Engineering Research, and the Institute of Advanced Machines and Design at Seoul National University.

Conflict of Interest

The authors declare no conflict of interest.

Author Contributions

M.-S.K. and S.-H.A. conceived the project. M.-S.K., H.-S.L. S.W.L., J.-K.H., and Y.-J.Q. carried out the experiment. Y.C. performed the FDTD simulation. S.-H.A. and H.J.P. supervised the project. All authors provided meaningful feedback for the project and manuscript.

Data Availability Statement

The data that support the findings of this study are available from the corresponding author upon reasonable request.

Keywords

actuators, artificial muscles, metasurfaces, plasmonic effects, shape memory alloys

Received: September 20, 2021

Revised: November 25, 2021

Published online: December 23, 2021

- [1] a) S. M. Mirvakili, I. W. Hunter, *Adv. Mater.* **2018**, *30*, 1704407; b) W.-S. Chu, K.-T. Lee, S.-H. Song, M.-W. Han, J.-Y. Lee, H.-S. Kim, M.-S. Kim, Y.-J. Park, K.-J. Cho, S.-H. Ahn, *Int. J. P. Eng. Manuf.* **2012**, *13*, 1281; c) S.-H. Song, M.-S. Kim, H. Rodrigue, J.-Y. Lee, J.-E. Shim, M.-C. Kim, W.-S. Chu, S.-H. Ahn, *Bioinspiration Biomimetics* **2016**, *11*, 036010; d) M. W. Han, S. H. Ahn, *Adv. Mater.* **2017**, *29*, 1606580; e) M.-W. Han, M.-S. Kim, S.-H. Ahn, *Composites, Part B* **2020**, *198*, 108170; f) W. Wang, C. Y. Yu, P. A. Abrego Serrano, S.-H. Ahn, *Soft Rob.* **2020**, *7*, 283.
- [2] M. Sitti, *Extreme Mech. Lett.* **2021**, *46*, 101340.
- [3] G. Mao, M. Drack, M. Karami-Mosammam, D. Wirthl, T. Stockinger, R. Schwödiauer, M. Kaltenbrunner, *Sci. Adv.* **2020**, *6*, eabc0251.
- [4] S. Nocentini, C. Parmeggiani, D. Martella, D. S. Wiersma, *Adv. Opt. Mater.* **2018**, *6*, 1800207.
- [5] a) H. Zeng, P. Wasylczyk, C. Parmeggiani, D. Martella, M. Burresti, D. S. Wiersma, *Adv. Mater.* **2015**, *27*, 3883; b) S. M. Mirvakili, A. Leroy, D. Sim, E. N. Wang, *Adv. Sci.* **2021**, *8*, 2004235.
- [6] a) M. Del Pozo, J. A. Sol, A. P. Schenning, M. G. Debije, *Adv. Mater.* **2021**, 2104390; b) D.-G. Shin, T.-H. Kim, D.-E. Kim, *Int. J. Precis. Eng. Manuf.-Green Technol.* **2017**, *4*, 349.
- [7] a) Y. Fu, H. Du, W. Huang, S. Zhang, M. Hu, *Sens. Actuators, A* **2004**, *112*, 395; b) J. Huber, N. Fleck, M. Ashby, *Proc. R. Soc. London, Ser. A* **1997**, *453*, 2185; c) H. Okamura, in *2010 Int. Symp. on Optomechatronic Technologies*, IEEE, Toronto, ON, Canada **2010**; d) G. K. Knopf, in *Proc. SPIE 5263, Intelligent Manufacturing*, SPIE, Bellingham, WA **2004**, pp. 22–29.
- [8] J. M. Jani, M. Leary, A. Subic, M. A. Gibson, *Mater. Des.* (1980-2015) **2014**, *56*, 1078.
- [9] H. T. Lee, M. S. Kim, G. Y. Lee, C. S. Kim, S. H. Ahn, *Small* **2018**, *14*, 1801023.
- [10] M. S. Kim, H. T. Lee, S. H. Ahn, *Adv. Mater. Technol.* **2019**, *4*, 1970064.
- [11] C. R. Knick, G. L. Smith, C. J. Morris, H. A. Bruck, *Sens. Actuators, A* **2019**, *291*, 48.
- [12] N. Patra, K. Akash, S. Shiva, R. Gagrani, H. S. P. Rao, V. Anirudh, I. Palani, V. Singh, *Appl. Surf. Sci.* **2016**, *366*, 104.
- [13] A. P. Malshe, S. Bapat, K. P. Rajurkar, H. Haitjema, *CIRP Ann.* **2018**, *67*, 627.
- [14] a) J. Scheuer, *ACS Photonics* **2020**, *7*, 1323; b) A. Kristensen, J. K. Yang, S. I. Bozhevolnyi, S. Link, P. Nordlander, N. J. Halas, N. A. Mortensen, *Nat. Rev. Mater.* **2016**, *2*, 15015.
- [15] W. L. Barnes, A. Dereux, T. W. Ebbesen, *Nature* **2003**, *424*, 824.
- [16] a) Y.-J. Quan, Y.-G. Kim, M.-S. Kim, S.-H. Min, S.-H. Ahn, *ACS Nano* **2020**, *14*, 5392; b) Y.-J. Quan, M.-S. Kim, Y. Kim, S.-H. Ahn, *CIRP Ann.* **2019**, *68*, 595; c) Y.-G. Kim, Y.-J. Quan, M.-S. Kim, Y. Cho, S.-H. Ahn, *Int. J. Precis. Eng. Manuf.-Green Technol.* **2021**, *8*, 997.
- [17] N. Yu, F. Capasso, *Nat. Mater.* **2014**, *13*, 139.
- [18] S. V. Boriskina, H. Ghasemi, G. Chen, *Mater. Today* **2013**, *16*, 375.
- [19] S. Zaidi, F. Lamarque, C. Prella, O. Carton, A. Zeinert, *Smart Mater. Struct.* **2012**, *21*, 115027.
- [20] a) H.-T. Lee, K.-I. Lee, K.-H. Jang, S.-H. Ahn, *Int. J. Precis. Eng. Manuf.* **2020**, *21*, 491; b) V. Garg, R. G. Mote, J. Fu, *Adv. Mater. Technol.* **2018**, *3*, 1800100; c) G. Seniutinas, A. Balčytis, I. Reklaitis, F. Chen, J. Davis, C. David, S. Juodkakis, *Nanophotonics* **2017**, *6*, 923.
- [21] Q. Wang, W. W. S. Yue, Z. Jiang, T. Xue, S. H. Kang, D. E. Bergles, K. Mikoshiba, S. Offermanns, K.-W. Yau, *Curr. Biol.* **2017**, *27*, 1791.
- [22] M. A. McEvoy, N. Correll, *Science* **2015**, *347*; *Nat. Mach. Intell.* **2020**, *2*, 653.
- [23] K. Yamaji, T. Yoshitomi, S. Usui, Y. Ohnishi, *Vision Res.* **2003**, *43*, 479.
- [24] a) V. Bell, W. A. Mitchell, S. Sigurðsson, J. J. Westenberg, J. D. Gotal, A. A. Torjesen, T. Aspelund, L. J. Launer, A. de Roos, V. Gudnason,

- J. Am. Heart Assoc.* **2014**, *3*, e001536; b) T. M. Rothermel, Z. Win, P. W. Alford, *J. Biomech.* **2020**, *111*, 110005.
- [25] S. Sung, C.-H. Kim, J. Lee, J.-Y. Jung, J.-h. Jeong, J.-H. Choi, E.-S. Lee, *Int. J. Precis. Eng. Manuf.-Green Technol.* **2014**, *1*, 25.
- [26] K. Kim, S. Kim, S. Kwon, H. J. Pakh, *Int. J. Precis. Eng. Manuf.* **2014**, *15*, 1817.
- [27] a) K. Bhattacharya, R. D. James, *Science* **2005**, *307*, 53; b) R. Pfeifer, M. Lungarella, F. Iida, *Science* **2007**, *318*, 1088.